Glioblastoma stem cell morphotypes convey distinct cell states and clinically relevant functions

Carlotta Barelli[1], Matteo Bonfanti[1]†, Filippo Mirabella[1]†, Dario Ricca[1], Negin Alizadehmohajer[1], Viktoria Sokolova[1], Alberto Campione[1,2], Giovanni M. Sicuri[2], Clelia Peano[1,3], Stefania Faletti[1], Roberto Stefini[2], Nereo Kalebic[1]*

Affiliations:

[1] Human Technopole, Milan, Italy

[2] Neurosurgery Unit, ASST Ovest Milanese - Legnano Hospital, Legnano, Italy

[3] Institute of Genetics and Biomedical Research, UoS of Milan, National Research Council, Milan, Italy

†Equal contribution

*Corresponding author: nereo.kalebic@fht.org

Abstract

Glioblastoma (GBM) is an aggressive brain tumor with a poor prognosis, driven by therapy resistance and invasion into healthy tissue. GBM stem cells (GSCs) play a central role in tumor progression, yet their biology remains poorly understood. Leveraging the similarities between GSCs and embryonic neural progenitor cells, we explore the relationship between GSC morphology and functional states. Combining a custom spatial transcriptomics approach with microscopy in patient-derived GBM organoids, we identified three distinct GSC morphoclasses—elongated, multipolar, and nonpolar—each with a unique transcriptional signature. These morphoclasses correspond to specific behaviors: while elongated cells are invasive, multipolar GSCs form networks conferring chemoresistance. Our findings establish a direct link between stem cell morphology and function, offering new insights into potential therapeutic strategies for invasion and chemoresistance in cancer.

Introduction

Glioblastoma (GBM) is the most common and aggressive brain tumor, representing an unmet clinical need, with a median survival rate of only 15 months (*1*). Characterized by extensive intra- and inter-tumoral heterogeneity, resistance to conventional therapies, and aggressive infiltration into healthy brain tissue, GBM almost inevitably relapses (*2, 3*). Central to these features are GBM stem cells (GSCs), a subpopulation driving tumor invasion and chemoresistance (*4-6*). Despite their pivotal role, the cell biology of GSCs remains poorly understood. GSC heterogeneity (*7*) and quiescence significantly contribute to their therapeutic resistance, especially to alkylating agents (*8*). Hence, a major challenge with GBM is to scrutinize GSC biology to reveal the underlying mechanisms contributing to their heterogeneity.

Transcriptional profiling has been valuable to extract the heterogeneity of cellular states in GBM and GSCs (*7, 9-11*), but is still unable to predict prognosis and comprehensively link clinically relevant functions to GSC states. Interestingly, GSCs share striking similarities with neural progenitor cells (*7, 12-14*), particularly basal or outer radial glia (bRG). In these progenitors, cell morphology is a critical feature for both their key functions: proliferation and serving as a scaffold for neuronal migration (*15*). Interestingly, for these functions, the interaction with the microenvironment appears to be critical (*15*). We recently observed that GSCs exhibit morphological heterogeneity, with morphotypes reminiscent of those seen in embryonic bRGs (*16*). Moreover, both GSCs and bRGs share specific morphoregulatory proteins, such as ADD3 (*16, 17*), highlighting potential mechanistic links. This prompts us to examine the GSC morphology in the context of their transcriptional and functional heterogeneity.

In GBM, morphological plasticity allows tumor cells to switch between rapid proliferation when environmental conditions favor growth and aggressive invasion when growth is restricted (*6*). Interestingly, GSCs also exhibit morphological stability. We have recently showed that the morphotype identity is both inhereted from mother to daughter cells and maintained throughout the interphase (*16*). This provides a basis to link specific cell morphologies with distinct functions in GBM. Moreover, GBM cells exhibit specialized cellular protrusions connecting tumor cells into a multicellular network that enhances tumor resilience and repair capacity (*18, 19*). While recent studies have suggested that morphological traits could predict functional behaviors in various cancer cell lines (*20-25*), these analyses predominantly relied on 2D cultures, which fail to fully recapitulate the complexities of in vivo environments, and were rarely focused on stem cells. Organoids, on the other hand, offer a more physiologically relevant system, containing both the cellular heterogeneity and the extracellular signals critical for the regulation of cell morphology. In this study, we use patient-derived GBM organoids, spatial biology, and functional assays to investigate how GSC morphological heterogeneity might be linked to distinct cellular behaviors.

GSCs are morphologically heterogeneous in patient-derived organoids

We generated patient-derived GBM organoids using a protocol which maintains the original 3D tumor architecture and native microenvironment without dissociation (*26*) (fig. S1A, Fig. 1A, B). Organoid viability was confirmed by markers for mitotic and actively cycling cells and lack of the apoptotic signals (fig. S1B, C). Using a panel of markers, we validated the presence of GSCs, along with neurons, astrocytes and fragments of blood vessels in GBM organoids (Fig. 1B, fig. S1D-G). For most future purposes, GSCs were identified as cells expressing both SOX2 and nestin (Fig. 1A, B). Using nestin signal to track cell shape, we identified six distinct GSC morphotypes, defined as categories of cells with specific and consistent morphological

features (Fig. 1C). We further grouped these morphotypes into three main morphoclasses (families of morphotypes with similar core features), comparably to what we previously established in 2D cancer cell lines (*16*). The three morphoclasses were: nonpolar (encompassing both flat and round nonpolar cells and accounting for ~20% of all GSCs), elongated (comprising radial and bipolar cells; ~30% of total) and multipolar (containing both flat and round nonpolar cells; ~50% of total) (Fig. 1C, D). Importantly, organoids faithfully recapitulated the morphological distribution of GSCs observed in patient samples for at least 15 weeks (Fig. 1D, fig. S1H-J), consistently with what previously reported for gene expression (*26*). Thus, GBM organoids recapitulate and maintain the morphological heterogeneity of GSCs, thereby providing a robust model to study its functional implications.

GSC morphoclasses have distinct transcriptomic signatures

To transcriptionally characterize individual morphoclasses, we performed spatial transcriptomics. While this technique has been valuable at integrating tissue morphology with cell identity and function (*27-29*), it has not been fully explored to utilize morphology of individual cells. We hence developed a custom spatial transcriptomics approach by adapting the GeoMX platform. Our approach consists of manual segmentation of individual cells belonging to different morphoclasses (Fig. 2A), followed by bulk RNA sequencing of morphoclass-specific transcriptomes from multiple patient-derived organoids. The analysis revealed patient-dependent clustering (Fig. 2B), consistent with previous reports in GBM (*9, 12*). To account for this, we performed pathway deconvolution analysis as done previously (*9*). This demonstrated that nonpolar GSCs are transcriptionally more distant from elongated and multipolar GSCs (Fig. 2C, D). Clustering with the Leiden algorithm further supported this separation, placing nonpolar cells apart from elongated and multipolar populations (Fig. 2E, F, fig. S2A). Such results prompted us to explore potential resemblance of Leiden clusters with four GBM subtypes, which embody developmental and metabolic attributes, as described previously (*9*). Functional scoring of pathway enrichment values linked nonpolar GSCs to neuronal-like GBM subtypes and elongated and multipolar cells to progenitor-like subtypes (Fig. 2G, H). In the context of the metabolic states, elongated and multipolar cells were associated to a GBM subtype dependent on oxidative phosphorylation (termed mitochondrial GBM state (*9*)), whereas nonpolar GSCs showed more resemblance to the glycolytic-plurimetabolic subtype (Fig. 2I, J), without however exhibit signature of metabolic plasticity associated with GBM aggressiveness (fig. S2). Considering that nonpolar GSCs showed greatest distance from the other morphoclasses, we performed differential expression analysis (fig. S2B). This showed that nonpolar GSCs exhibit significantly reduced expression of both protein translation genes, potentially linked to their smaller size, and genes involved in oxidative phosphorylation, in line with analysis of GBM subtypes (fig. S2C).

These results indicate that GSC morphoclasses correspond to distinct transcriptomic states reflective of clinically relevant distribution of GBM subtypes. Given the greatest resemblance of elongated and multipolar GSCs to progenitor-like GBM state and their more complex morphology, we next south to functionally examine these subpopulations.

Elongated GSCs are invasive and associated to blood vessels

Differential gene expression analysis comparing elongated GSCs to other morphoclasses revealed significant enrichment in genes related to cell migration and adhesion (Fig. 3A, fig.S3A, B). We put these results in the context of previous studies suggesting that cell elongation can predict invasiveness across various cancer cell types (*30, 31*). Among the genes enriched in elongated GSCs, we detected CD99 (fig. S3C), previously implicated in GBM

invasiveness and cell elongation (*32, 33*), and observed accumulation of CD99+ cells along the blood vessels in our tumor samples (fig. S3D).

Given that invading GBM cells frequently use vasculature as migratory paths (*34-37*), we investigated the relationship between elongated GSCs and blood vessel fragments in our culture systems. Microscopy analysis showed that these cells account for around 80% of vessel-attached GSCs both in GBM tissue and organoids, whereas they comprise only around 30% of total GSCs (Fig. 3B-D), indicating a strong enrichment of elongated GSCs around blood vessels. This prompted us to examine a potential role of elongated GSCs in invasiveness, taking advantage of the differences in GBM samples from the core *vs* the periphery of the tumor. Spatial analysis by immunofluorescence showed a remarkable enrichment of elongated GSCs in the GBM periphery compared to the core (Fig. 3E, F). Next, we specifically focused on the invasive niche (*38, 39*), which we identified through enrichment for neuronal, microglia and metalloproteinase markers (fig. S3E, F). Analysis of the morphoclass distribution in the invasive niche showed a striking enrichment of elongated GSCs (fig. S3G, H). Together, these data suggest a strong spatial enrichment of elongated cells in tumor regions implicated in invasiveness.

Hence, we functionally assessed the involvement of elongated GSCs in GBM invasiveness using invasion assays in assembloids. While previous assembloid models mostly fuse GBM organoids with developing cortical organoids lacking vasculature (*40-43*), we fused them with peripheral tumor organoids, which do contain fragments of blood vessels. We labeled GBM cells in the core with EdU and examined their invasion into the peripheral organoid ten days post fusion (Fig. 3G, H, fig. S3I). The relative distribution of morphoclasses among EdU+ cells in the core organoid was comparable to untreated controls (compare Fig. 3I core and 3F core), indicating no bias in S-phase progression across morphoclasses. Strikingly, despite representing ~30% of GSCs in the core, the elongated EdU+ GSCs accounted for ~50% of cells invading into the peripheral organoid (Fig. 3I). Furthermore, vessel-associated EdU+ GSCs doubled in proportion in the invaded periphery compared to the core (Fig. 3J-L). These functional assays in assembloids strongly support that elongated GSCs drive invasion along blood vessels, consistent with their transcriptional profile and localization within the tumor niches.

Multipolar GSCs form functional resistant networks

Transcriptomic analysis revealed that multipolar GSCs exhibit enrichment in genes related to morphoregulation, growth of cell protrusions and calcium signaling (Fig. 4A, fig. S4A, B). We link these data with the notion that GBM cells form a network of inter-cellular connections that are important for maintaining the aggressive and chemoresistant nature of the tumor (*16, 19, 44, 45*). Such connections, mediated by tumor microtubes and tunneling nanotubes, enable inter-cellular communication through calcium signaling (*18, 46-48*), similar to calcium waves in radial glia during neurodevelopment (*49, 50*). We hence sought to examine the relative contribution of multipolar cells to such networks in GBM organoids.

We performed live calcium imaging in GBM organoids using Fluo4 sensor and analyzed the morphology of the firing cells (Fig. 4B). Remarkably, almost 80% of the active cells were multipolar (Fig. 4C and compare to fig. S4C). Previous study (*48*) identified GBM cells displaying rhythmic calcium oscillations that trigger calcium waves within tumor cell networks (trigger cells), serving as hubs for intercellular communication (hub cells). By mapping calcium connectivity, we observed that multipolar cells predominantly act as trigger and hub cells, further emphasizing their fundamental role in GBM networks (Fig. 4D-F). Such

connections between GBM cells are often mediated through gap junctions (*18, 51*). We confirmed through immunostaining for connexin-43 (Cx43) that multipolar GSCs in GBM organoids are connected through gap junctions (fig. S4D).

Multicellular networks in GBM have been strongly implicated in therapeutic resistance (*18, 52-54*), particularly through gap junction-mediated intercellular communication (*55, 56*). We previously demonstrated that the morphoregulatory protein adducin-3 (ADD3) promotes both connections between GSCs and resistance to temozolomide (TMZ), the main GBM chemotherapeutic (*16*). To explore the contribution of multipolar GSCs to this connectivity-mediated resistance, we examined TMZ-resistant cells in a GSC line and found that the majority of surviving cells indeed displayed a multipolar morphology (fig. S5A-C). Next, we treated GBM organoids with TMZ (fig. S5D) and consistently detected an enrichment of multipolar cells at the expense of nonpolar GSCs after 10 days of metronomic treatment (Fig. 4G, H). Collectively, these results suggest that multipolar GSCs exhibit a transcriptomic signature of protrusion growth and calcium signaling and are involved in establishment of functional gap junction-mediated intercellular networks that promote resistance to chemotherapy.

Conclusion

Our study establishes a direct link between GSC morphology, transcriptional identity, and clinically relevant functions, such as invasion and chemoresistance—two key challenges in the clinical management of GBM. Our findings align with the previous studies implying that GBM cell morphology is associated with proliferation, invasiveness and chemoresistance (*6, 37, 57-59*). By focusing on GSCs in 3D organoids, our study reveals a clear link between morphology and transcriptional states associated with clinically relevant metabolic and developmental GBM subtypes (*9, 60*). The stability or flexibility of the identified morphoclasses remains to be further elucidated. Microenvironmental conditions were shown to induce reversible morphological switches in GBM cells (*61*), however, recent live imaging data suggest that some morphological features are stably inherited from mother to daughter GSCs (*16*). Importantly, we show that elongated GSCs are primarily implicated in tumor invasiveness along the blood vessels, while multipolar cells are involved in generation of multicellular networks which confer resistance to chemotherapy. Such networks are a paradigmatic example of how a morphological feature – the presence of cellular protrusions and thus intercellular connections – directly augments GSC survival as cells collectively resist therapies that would kill them individually (*16, 18, 52*). This underscores GSC morphology as a clinically functional trait.

In summary, our findings demonstrate that intrinsic variability in GSC morphology is linked with the critical aspects of GBM aggressiveness. This shows the necessity of moving beyond traditional cytotoxic treatments towards strategies that target the physical and phenotypic adaptations of the tumor. Morphology-informed therapies—such as disrupting cytoskeletal regulators critical for maintaining complex and protective GSC morphologies or blocking the formation of intercellular networks via gap junction inhibitors could show promise in this context (*62, 63*). We hence propose that integrating these morphological insights into treatment design might improve responses to therapy and patient outcomes.

References and Notes

1. B. Tran, M. A. Rosenthal, Survival comparison between glioblastoma multiforme and other incurable cancers. *J Clin Neurosci* **17**, 417-421 (2010).
2. L. Marenco-Hillembrand *et al.*, Trends in glioblastoma: outcomes over time and type of intervention: a systematic evidence based analysis. *J Neurooncol* **147**, 297-307 (2020).
3. R. Stupp *et al.*, Radiotherapy plus concomitant and adjuvant temozolomide for glioblastoma. *N Engl J Med* **352**, 987-996 (2005).
4. R. C. Gimple, S. Bhargava, D. Dixit, J. N. Rich, Glioblastoma stem cells: lessons from the tumor hierarchy in a lethal cancer. *Genes Dev* **33**, 591-609 (2019).
5. G. Liu *et al.*, Analysis of gene expression and chemoresistance of CD133+ cancer stem cells in glioblastoma. *Mol Cancer* **5**, 67 (2006).
6. Q. Xie, S. Mittal, M. E. Berens, Targeting adaptive glioblastoma: an overview of proliferation and invasion. *Neuro Oncol* **16**, 1575-1584 (2014).
7. C. Neftel *et al.*, An Integrative Model of Cellular States, Plasticity, and Genetics for Glioblastoma. *Cell* **178**, 835-849 e821 (2019).
8. X. P. Xie *et al.*, Quiescent human glioblastoma cancer stem cells drive tumor initiation, expansion, and recurrence following chemotherapy. *Dev Cell* **57**, 32-46 e38 (2022).
9. L. Garofano *et al.*, Pathway-based classification of glioblastoma uncovers a mitochondrial subtype with therapeutic vulnerabilities. *Nat Cancer* **2**, 141-156 (2021).
10. Q. Wang *et al.*, Tumor Evolution of Glioma-Intrinsic Gene Expression Subtypes Associates with Immunological Changes in the Microenvironment. *Cancer Cell* **32**, 42-56 e46 (2017).
11. K. Yu *et al.*, Surveying brain tumor heterogeneity by single-cell RNA-sequencing of multi-sector biopsies. *Natl Sci Rev* **7**, 1306-1318 (2020).
12. C. P. Couturier *et al.*, Single-cell RNA-seq reveals that glioblastoma recapitulates a normal neurodevelopmental hierarchy. *Nat Commun* **11**, 3406 (2020).
13. A. Bhaduri *et al.*, Outer Radial Glia-like Cancer Stem Cells Contribute to Heterogeneity of Glioblastoma. *Cell Stem Cell* **26**, 48-63 e46 (2020).
14. R. Azzarelli, B. D. Simons, A. Philpott, The developmental origin of brain tumours: a cellular and molecular framework. *Development* **145**, (2018).
15. N. Kalebic, W. B. Huttner, Basal Progenitor Morphology and Neocortex Evolution. *Trends Neurosci*, (2020).
16. C. Barelli *et al.*, Morphoregulatory ADD3 underlies glioblastoma growth and formation of tumor-tumor connections. *Life Sci Alliance* **8**, (2025).
17. N. Kalebic *et al.*, Neocortical expansion due to increased proliferation of basal progenitors is linked to changes in their morphology. *Cell Stem Cell* **24**, 535-550 (2019).
18. M. Osswald *et al.*, Brain tumour cells interconnect to a functional and resistant network. *Nature* **528**, 93-98 (2015).
19. G. Pinto, C. Brou, C. Zurzolo, Tunneling Nanotubes: The Fuel of Tumor Progression? *Trends Cancer* **6**, 874-888 (2020).
20. P. H. Wu *et al.*, Single-cell morphology encodes metastatic potential. *Sci Adv* **6**, eaaw6938 (2020).
21. C. G. Barker *et al.*, Identification of phenotype-specific networks from paired gene expression-cell shape imaging data. *Genome research* **32**, 750-765 (2022).

22. E. Alizadeh *et al.*, Cellular morphological features are predictive markers of cancer cell state. *Comput Biol Med* **126**, 104044 (2020).
23. R. Sali, Y. Jiang, A. Attaranzadeh, B. Holmes, R. Li, Morphological diversity of cancer cells predicts prognosis across tumor types. *J Natl Cancer Inst* **116**, 555-564 (2024).
24. Q. Da *et al.*, Quantifying the cell morphology and predicting biological behavior of signet ring cell carcinoma using deep learning. *Scientific reports* **12**, 183 (2022).
25. S. J. Conner *et al.*, Cell morphology best predicts tumorigenicity and metastasis in vivo across multiple TNBC cell lines of different metastatic potential. *Breast Cancer Res* **26**, 43 (2024).
26. F. Jacob *et al.*, A Patient-Derived Glioblastoma Organoid Model and Biobank Recapitulates Inter- and Intra-tumoral Heterogeneity. *Cell* **180**, 188-204 e122 (2020).
27. B. L. Walker, Z. Cang, H. Ren, E. Bourgain-Chang, Q. Nie, Deciphering tissue structure and function using spatial transcriptomics. *Commun Biol* **5**, 220 (2022).
28. F. Bao *et al.*, Integrative spatial analysis of cell morphologies and transcriptional states with MUSE. *Nat Biotechnol* **40**, 1200-1209 (2022).
29. T. Song *et al.*, Predicting spatially resolved gene expression via tissue morphology using adaptive spatial GNNs. *Bioinformatics* **40**, ii111-ii119 (2024).
30. J. P. Baskaran *et al.*, Cell shape, and not 2D migration, predicts extracellular matrix-driven 3D cell invasion in breast cancer. *APL Bioeng* **4**, 026105 (2020).
31. A. Fayzullin *et al.*, Time-lapse phenotyping of invasive glioma cells ex vivo reveals subtype-specific movement patterns guided by tumor core signaling. *Exp Cell Res* **349**, 199-213 (2016).
32. L. C. Cardoso *et al.*, CD99 Expression in Glioblastoma Molecular Subtypes and Role in Migration and Invasion. *Int J Mol Sci* **20**, (2019).
33. H. J. Seol *et al.*, Overexpression of CD99 Increases the Migration and Invasiveness of Human Malignant Glioma Cells. *Genes Cancer* **3**, 535-549 (2012).
34. S. Watkins *et al.*, Disruption of astrocyte-vascular coupling and the blood-brain barrier by invading glioma cells. *Nat Commun* **5**, 4196 (2014).
35. B. Krusche *et al.*, EphrinB2 drives perivascular invasion and proliferation of glioblastoma stem-like cells. *eLife* **5**, (2016).
36. G. J. Baker *et al.*, Mechanisms of glioma formation: iterative perivascular glioma growth and invasion leads to tumor progression, VEGF-independent vascularization, and resistance to antiangiogenic therapy. *Neoplasia* **16**, 543-561 (2014).
37. P. Monzo *et al.*, Mechanical confinement triggers glioma linear migration dependent on formin FHOD3. *Mol Biol Cell* **27**, 1246-1261 (2016).
38. D. Hambardzumyan, G. Bergers, Glioblastoma: Defining Tumor Niches. *Trends Cancer* **1**, 252-265 (2015).
39. L. Barthel *et al.*, Glioma: molecular signature and crossroads with tumor microenvironment. *Cancer Metastasis Rev* **41**, 53-75 (2022).
40. J. G. Roth *et al.*, Spatially controlled construction of assembloids using bioprinting. *Nat Commun* **14**, 4346 (2023).
41. Y. Liang *et al.*, CD146 increases stemness and aggressiveness in glioblastoma and activates YAP signaling. *Cell Mol Life Sci* **79**, 398 (2022).
42. B. da Silva, R. K. Mathew, E. S. Polson, J. Williams, H. Wurdak, Spontaneous Glioblastoma Spheroid Infiltration of Early-Stage Cerebral Organoids Models Brain Tumor Invasion. *SLAS Discov* **23**, 862-868 (2018).
43. J. Kim *et al.*, Assembly of glioblastoma tumoroids and cerebral organoids: a 3D in vitro model for tumor cell invasion. *Mol Oncol* **19**, 698-715 (2025).

44. V. Venkataramani *et al.*, Disconnecting multicellular networks in brain tumours. *Nat Rev Cancer* **22**, 481-491 (2022).
45. L. Hai *et al.*, A clinically applicable connectivity signature for glioblastoma includes the tumor network driver CHI3L1. *Nat Commun* **15**, 968 (2024).
46. J. Y. Vargas *et al.*, The Wnt/Ca(2+) pathway is involved in interneuronal communication mediated by tunneling nanotubes. *The EMBO journal* **38**, e101230 (2019).
47. I. F. Smith, J. Shuai, I. Parker, Active generation and propagation of Ca2+ signals within tunneling membrane nanotubes. *Biophys J* **100**, L37-39 (2011).
48. D. Hausmann *et al.*, Autonomous rhythmic activity in glioma networks drives brain tumour growth. *Nature* **613**, 179-186 (2023).
49. T. A. Weissman, P. A. Riquelme, L. Ivic, A. C. Flint, A. R. Kriegstein, Calcium waves propagate through radial glial cells and modulate proliferation in the developing neocortex. *Neuron* **43**, 647-661 (2004).
50. B. G. Rash *et al.*, Metabolic regulation and glucose sensitivity of cortical radial glial cells. *Proc Natl Acad Sci U S A* **115**, 10142-10147 (2018).
51. M. Sinyuk, E. E. Mulkearns-Hubert, O. Reizes, J. Lathia, Cancer Connectors: Connexins, Gap Junctions, and Communication. *Front Oncol* **8**, 646 (2018).
52. S. Weil *et al.*, Tumor microtubes convey resistance to surgical lesions and chemotherapy in gliomas. *Neuro Oncol* **19**, 1316-1326 (2017).
53. M. D. Kolba *et al.*, Tunneling nanotube-mediated intercellular vesicle and protein transfer in the stroma-provided imatinib resistance in chronic myeloid leukemia cells. *Cell Death Dis* **10**, 817 (2019).
54. Y. Hekmatshoar, J. Nakhle, M. Galloni, M. L. Vignais, The role of metabolism and tunneling nanotube-mediated intercellular mitochondria exchange in cancer drug resistance. *Biochem J* **475**, 2305-2328 (2018).
55. A. L. Potthoff *et al.*, Inhibition of Gap Junctions Sensitizes Primary Glioblastoma Cells for Temozolomide. *Cancers (Basel)* **11**, (2019).
56. L. Wang *et al.*, Tramadol attenuates the sensitivity of glioblastoma to temozolomide through the suppression of Cx43-mediated gap junction intercellular communication. *Int J Oncol* **52**, 295-304 (2018).
57. V. Venkataramani *et al.*, Glioblastoma hijacks neuronal mechanisms for brain invasion. *Cell* **185**, 2899-2917 e2831 (2022).
58. M. Ratliff *et al.*, Individual glioblastoma cells harbor both proliferative and invasive capabilities during tumor progression. *Neuro Oncol*, (2023).
59. K. P. L. Bhat *et al.*, Mesenchymal differentiation mediated by NF-kappaB promotes radiation resistance in glioblastoma. *Cancer Cell* **24**, 331-346 (2013).
60. C. Bernhard, D. Reita, S. Martin, N. Entz-Werle, M. Dontenwill, Glioblastoma Metabolism: Insights and Therapeutic Strategies. *Int J Mol Sci* **24**, (2023).
61. C. F. Gao *et al.*, Proliferation and invasion: plasticity in tumor cells. *Proc Natl Acad Sci U S A* **102**, 10528-10533 (2005).
62. E. N. C. Schmidt *et al.*, Tonabersat enhances temozolomide-mediated cytotoxicity in glioblastoma by disrupting intercellular connectivity through connexin 43 inhibition. *Mol Oncol* **19**, 878-898 (2025).
63. T. Zeyen *et al.*, Phase I/II trial of meclofenamate in progressive MGMT-methylated glioblastoma under temozolomide second-line therapy-the MecMeth/NOA-24 trial. *Trials* **23**, 57 (2022).
64. M. D. Robinson, A. Oshlack, A scaling normalization method for differential expression analysis of RNA-seq data. *Genome biology* **11**, R25 (2010).

65. B. Muzellec, M. Telenczuk, V. Cabeli, M. Andreux, PyDESeq2: a python package for bulk RNA-seq differential expression analysis. *Bioinformatics* **39**, (2023).
66. C. Gene Ontology *et al.*, The Gene Ontology knowledgebase in 2023. *Genetics* **224**, (2023).
67. Z. Fang, X. Liu, G. Peltz, GSEApy: a comprehensive package for performing gene set enrichment analysis in Python. *Bioinformatics* **39**, (2023).
68. A. Liberzon *et al.*, Molecular signatures database (MSigDB) 3.0. *Bioinformatics* **27**, 1739-1740 (2011).
69. F. A. Wolf, P. Angerer, F. J. Theis, SCANPY: large-scale single-cell gene expression data analysis. *Genome biology* **19**, 15 (2018).

Acknowledgments: We are grateful to the services and facilities of HT for the outstanding support provided, notably, N. Maghelli and the team of the National Facility (NF) for Light Imaging, including the infrastructural units (IU) for Ion imaging and Tissue processing, A. Riva and the team of the NF for Data Handling and Analysis, including D. dalle Nogare and the team of the IU for Bioimage analysis, and the team of the NF for Genomics. We thank all members of the Kalebic laboratory for their support and discussions. CB is a Ph.D. student within the European School of Molecular Medicine (SEMM).

Funding:

AIRC grant MFAG 2022 ID 27157 (NK)

Funds of the Human Technopole (NK)

Author contributions:

Conceptualization: CB, NK

Methodology: CB, MB, FM, DR, SF, CP

Investigation: CB, FM, NA, VS, SF

Formal analysis: CB, MB, FM

Visualization: CB, MB, FM

Resources: AC, GMS, RS

Funding acquisition: NK

Project administration: NK

Supervision: NK

Writing – original draft: CB, NK

Writing – review & editing: all authors

Competing interests: Authors declare that they have no competing interests.

Materials and Methods

Human samples

Glioblastoma patient samples were obtained from Ospedale Nuovo di Legnano following informed patient consent. A total of 14 patient samples from both males and females between

43 and 82 years old with a diagnosis of grade IV astrocytoma were included. Fresh surgical resections were collected in Hibernate™-A Medium (A1247501, Thermo Fisher) containing Penicillin/Streptomycin 100X (ECB3001D, Euroclone) and Amphotericin B 100X (15290018, Thermo Fisher) and transported to Human Technopole at 4°C for processing. Immediately upon arrival, the tissue was dissected in Hibernate™-A Medium and washed with the same medium to remove cellular debris. For each patient sample most of the tissue was further processed to generate patient-derived glioblastoma organoids, some was snap frozen and the remaining was fixed in 4% paraformaldehyde (PFA) After 24h of fixation, the tissue was left in 15% and 30% sucrose gradients for 24 h each. Following embedding in OCT compound Killik (05-9801, Bio Optica), serial sections of 20 µm were cut at the cryostat and stored at -20°C for immunofluorescence experiments. For most patients we obtained both core and peripheral tissue, with the core exhibiting high and the periphery low 5-ALA signal intensity during surgical resection. From those tumor samples we generated both organoids and fixed frozen sections for immunofluorescence.

GBM organoid generation and culture

The dissected surgical specimens were cut into small pieces (0.5 to 1 mm diameter) with microdissection scissors and incubated in 1X RBC Lysis Buffer (00-4333-57, Thermo Fisher) for 10 minutes in shaking, following the previously established protocol (*26*). After washing with Hibernate™-A medium, the dissected pieces were cultured in 6-well low attachment plates (Corning, 3471) in their GBO medium composed of 50% DMEM:F12 (Thermo Fisher Scientific, 11330057), 50% Neurobasal (Thermo Fisher Scientific, 21103049), 1X GlutaMax (Thermo Fisher Scientific, 35050038), 1X NEAAs (Thermo Fisher Scientific, 11140050), 1X PenStrep (ECB3001D, Euroclone), 1X N2 supplement (Life Technologies, 17502-048), 1X B27 (Thermo Fisher Scientific, 17504001), 1X 2-mercaptoethanol (Sigma Aldrich, M6250-100ML), and 2.5 µg/ml human insulin (Sigma Aldrich, I0516) and placed on an orbital shaker rotating at 120 rpm within a 37°C, 5% CO2, and 90% humidity sterile incubator. The organoids generally form within 2-4 weeks and were then used for experiments up to week 15 of culture.

Immunofluorescence

For immunofluorescence of human glioblastoma tissue and organoids, antigen retrieval was performed by incubating the slides for 45 min with 10 mM citrate buffer pH6.0 in 70°C oven. Following three washes in PBS, the tissue was permeabilized for 30 min in 0.3% Triton X-100 at room temperature, quenching for 30 min in 0.1 M glycine in PBS at room temperature and blocking for 30 min in blocking solution containing 10% normal donkey serum (Jackson ImmunoResearch, 017-000-121), 300 mM NaCl, 0.5% Triton X-100 in PBS. Primary antibodies Anti-Nestin (1:500, Invitrogen, MA1-110), Anti-SOX2 (1:200, R&D, AF2018), Anti-Laminin (1:500, Sigma Aldrich, L9393), Anti-Ki67 (1:500, Cell Signaling Technologies, 129S), Anti-Connexin43 (1:500, Sigma, C6219), Anti-GFAP (1:1000, Dako, Z0334), Anti-HuC/D (1:500, Abcam, ab184267), Anti-IBA1 (1:500, Synaptic Systems, 234 308), Anti-TuJ1 (1:500, Biolegend, 801202), Anti-MMP2 (1:200, Abcam, ab92536), Anti-Vimentin (1:500, Sigma, V5255), Anti-CD44 (1:500, Invitrogen, MA4400), Anti-cleaved Casp3 (1:200, Abcam, ab2302), Anti-SALL4 (1:200, Abcam, Ab29112), Anti-OCT4 (1:200, Abcam, Ab19857), Anti-PH3 (1:500, Abcam, ab10543) were incubated in blocking solution for 12 h, at 4°C. Following three washes in PBS, the sections were incubated with secondary antibodies Alexa Fluor PLUS (1:500, Thermo Fisher) and DAPI (1:2000, Thermo Fisher, 62248) in 0.3% Triton X-100 in PBS for 1 h at room temperature, washed again 3 times in PBS and mounted on

microscopy slides with Mowiol 4-88 (Sigma Aldrich, 81381) + DABCO (antifade, Sigma Aldrich, D27802).

Microscopy and image analysis

Microscopy of fixed samples was performed a Zeiss Axioscan z.1 slide scanner for overview images of whole organoids and confocal microscopes Zeiss LSM980 point-scanning confocal or LSM980-NLO point-scanning confocal or a Nikon Ti2-CREST spinning disk confocal microscope for other images. The confocal images were acquired with a PlanApo 10X/0.45 dry or a PlanApo 20X/0.8 dry or a PlanApo 40X/1.4 NA oil immersion objectives using 405nm, 488 nm, 561 nm, 639 nm laser lines. The software used for all acquisitions was Zen Blue 3.7 (Zeiss) or NIS-Elements (Nikon). Once the parameters of acquisition for control conditions had been defined, they were kept constant for all the samples within the same experiment. For live imaging and the associated analysis see below "Calcium imaging and analysis".

All manual cell quantifications were performed in Fiji ImageJ using the CellCounter function, processed with Microsoft Excel, and plotted in GraphPad Prism. Morphotypes and morphoclasses were assigned for GSCs identified as Nestin+ SOX2+ cells in both primary tissue and organoids. For quantification of GSCs associated to blood vessels, we considered all Nes+ SOX2+ cells whose Nes+ was in contact with Laminin+ vessels. For assembloid invasion, we assigned morphoclasses to all EdU+ Nes+ SOX2+ cells in the core of the assembloid and in the invaded periphery. For histological sections, the labelling of core and peripheral tumor tissue came from the surgeons and the pathologists. For quantification of resistant Onda-11 GSC populations, morphoclasses were assigned to the cells at day 7 using bright field images and following the morphological classification we have established previously (*16*). For the TMZ experiments in organoids, we quantified the morphoclass distribution of Nes+ SOX2+ cells after 10 days of metronomic TMZ administration.

Customized GeoMX spatial transcriptomics

Four GBM organoids from each of the four different selected patients were formalin fixed paraffin embedded (FFPE). After fixation in 10% NBF (Bio-Optica, 05-01004F) for 24 hours at room temperature and washes in PBS, the organoids were embedded in 2% low melting agarose (Invitrogen, 16520050). For paraffin embedding, the automatic tissue processor Sakura Tissue-Tek VIP6 was used. The paraffin blocks were cut on the microtome at 4 µm thickness. Slide preparation for GeoMX was carried out as instructed by the GeoMx DSP Manual Slide Preparation (MAN-10150-06). Briefly, the FFPE organoid sections were deparaffinized and rehydrated with Xylene, 100% EtOH, 95% EtOH, and DEPC-treated water. Antigen retrieval was performed with Tris-EDTA pH9 for 10 minutes at 99°C, followed by the exposure of RNA targets through Proteinase K 0,1 µg/ml for 15 min at 37°C. The sections were post-fixed in 10% NBF (Bio-Optica, 05-01004F) before the in situ hybridization with the Human Whole Transcriptome Atlas probe-set (GMX-RNA-NGS-HuWTA-4) would take place overnight in the hybridization oven (HybEZ II, ACDbio). Stringent washes were performed in a solution of 2X SSC and 50% formamide to remove off target probes. After blocking the non-specific staining with Buffer W provided by the company, the morphology markers were added by diluting the primary antibodies Anti-Nestin (1:500, Invitrogen, MA1-110) and Anti-SOX2 (1:200, R&D AF2018) in the same buffer. Following 1-hour incubation at room temperature the sections were washed in 2X SSC and the secondary antibodies Alexa Fluor PLUS Anti-Goat 555 (1:500, Invitrogen, A32816) and Anti-Mouse 647 (1:500, Invitrogen, A32787) along with the nuclear marker SYTO13 were added for 30 minutes at room temperature. Following washes in 2X SSC, the slides were stored in 2X SSC overnight at 4°C.

The following morning the slides were loaded and scanned by the NanoString GeoMX DSP machine. 16 ROIs (regions of interest) of the maximum size 660x785 µm (one per each

organoid covering almost the entire organoid) were drawn, downloaded and opened into FiJi. After adjusting the scale to the same as the GeoMX platform, the AOI (area of interest) single-cell segmentations were drawn using the free hand line tool around each of the desired Nestin+ SOX2+ cell. For each ROI, three separate masks, each for one of three morphoclasses (nonpolar, elongated, multipolar) was created, saved as .jpg files and re-uploaded onto the GeoMX platform. This resulted in 16 ROIs each one with three different AOI segmentations corresponding to the three morphoclasses of interest within each organoid.

Library preparation and sequencing

Oligos from selected AOIs were collected into a 96 well plate and were amplified and tagged with ROI-specific barcodes during library preparation, adding sequencing adapters for subsequent high-throughput sequencing, following the protocol described in the GeoMX DSP NGS Readout User Manual (MAN-10153-06).

Libraries were sequenced on a NextSeq2000 instrument (Illumina) generating per each AOI a number of reads pairs derived by applying the following formula n. read pairs = total collection area (μm^2) * sequencing depth factor (equal to 100 for the WTA panel).

Spatial transcriptomics sequencing analysis

Raw sequencing reads were processed using the GeoMx NGS Pipeline (NanoString, version 2.3.3.10) for alignment, deduplication, and quantification of the probes from the GeoMx Human Whole Transcriptome Atlas. To account for differences in sequencing depth, count data were normalized across AOIs using size factors computed via the trimmed mean of M values (TMM) method (*64*). Principal Component Analysis (PCA) was performed on the standardized data using scikit-learn v1.3.2 [https://scikit-learn.org/].

Differential expression analysis was conducted using PyDESeq2 v0.4.1 (*65*) on raw counts. A model was fitted, incorporating the patient of origin of the organoid and the AOI morphoclass as covariates. Gene expression contrasts were computed for each morphoclass (nonpolar, elongated, and multipolar) against the other two. Genes with an adjusted p-value < 0.05 were considered significantly differentially expressed. Significantly differentially expressed genes were functionally characterized through over-representation analysis of Biological Process Gene Ontology (GO) terms (2023 version (*66*)). Enrichment analysis was performed using the enrichr function from gseapy (*67*).

Biological pathway deconvolution analysis and GBM subtypes alignment

To further characterize the transcriptomic dataset, a pathway deconvolution analysis was performed following an approach similar to that described in Garofano et al. (*9*). The main points of this approach are:

1. Reduce inter-patient variability by standardizing gene expression within each patient group.
2. Perform single-sample pathway enrichment analysis using the Mann–Whitney–Wilcoxon Gene Set Test (MWW-GST).

More specifically, for each AOI gene expression was standardized within the patient subgroup to generate an AOI-specific ranked list of genes. A collection of gene sets was curated by merging: Hallmark, Gene Ontology, Oncogenic Signatures, KEGG MEDICUS, and Reactome pathways from the Molecular Signatures Database (MSigDB) (*68*). Gene sets containing fewer than 6 or more than 200 genes were excluded.

For each AOI, the Normalized Enrichment Scores (NES) for all selected gene sets were computed using a Mann-Whitney U test, comparing the ranks of genes in each pathway to background genes. The NES represents the probability that, in a given AOI, a randomly chosen

gene from the gene set ranks higher than a randomly chosen background gene. The NES was calculated from Mann-Whitney U using the following formula: NES = U/nm
with n being the number of genes in the gene list and m being the number of background genes. With each AOI now represented by a vector of NES values, a pathway-based embedding of the dataset was generated through dimensionality reduction. The 500 gene sets with the highest dispersion in NES values were selected. In this reduced space, the dataset was represented first by a nearest-neighbors graph constructed using k-nearest neighbors (k-NN) and then by a Uniform Manifold Approximation and Projection (UMAP) embedding, both obtained using functions from scanpy (*69*). Clustering was then performed using the Leiden algorithm with a standard resolution of 1.0, grouping AOIs based on NES similarity.
To further characterize the identified clusters in the context of glioblastoma transcriptomic profiles, we generated functional scores based on the classification proposed in (*9*). Specifically, we extracted four sets of gene pathways corresponding to the biological programs described in their single-cell analysis of glioblastoma tissue: Proliferative/Progenitor, Neuronal, Mitochondrial, and Glycolytic/Plurimetabolic. For each AOI, we computed a functional score for each of these biological classes by averaging the NES of the associated pathways. The final scores were computed using the score_genes function from scanpy.

Assembloid invasion assay

Assembloids were generated by fusing a core and a peripheral GBM organoids from the same patient. The two organoids were kept in a 1.5 ml Eppendorf for 5-7 days until when they were completely fused, meaning that they would not break when pipetting up and down the media. After fusion the assembloids were transferred into a low-attachment 6-well or 24-well plate until fixation in 4% PFA.
For invasion assays, before assembloid formation the core GBM organoids were treated with EdU for 24 hours so that multiple cells would uptake EdU. Following washes in PBS, they were fused with their corresponding peripheral organoid as described above. At day 15 (5 days in Eppendorf + 10 days in low attachment plates, i.e. 10 days post fusion), the assembloids were fixed and processed into 30µm cryosections as described above to analyse the EdU+ core cells which had invaded the peripheral part of the assembloid. For EdU detection by immunofluorescence, Click-iT™ EdU Cell Proliferation Kit for Imaging, Alexa Fluor™ 647 dye (Thermo Fisher, C10340) was used. These invasion assays were performed on two different assembloid batches, each containing at least four patients with 2-4 assembloids per patient.

Calcium imaging and analysis

GBM organoids were treated with Fluo4 AM Ca2+ indicator (Invitrogen, F14201) at 2 µM diluted in GBO media for 2 hours. Following three washes in GBM organoid media, the organoids were transferred to an IBIDI µ-Slide 8 Well and taken to the Nikon Ti2 - CrestOptics V3 spinning disk microscope for live imaging. To attach the organoids to the bottom of the dish, a homemade manufactured anchor was put on top of the organoid for the duration of the movie. Live imaging was performed at 37 °C with 5% CO2 and 3-5 minutes widefield movies were taken with a PlanApo 20X/0.8 dry using 488 nm laser lines with an acquisition frame rate of 5.05 frames/second. 2-6 organoids for each of the six different patients were used to obtain 1-4 movies per organoid.
To inhibit the calcium activity, a gap junction blocker Carbenoxolone (CBX) (Sigma Aldrich, C4790) was incubated at 100 µM for 15 minutes, after which another 3-5 minutes movie was taken in the same field of view where the activity was originally recorded.
The script for the analysis of calcium activity was adapted from (*48*). Briefly, ROIs of single cells were automatically segmented using a Fiji macro with the following steps "Auto Local

Threshold- Otsu method, radius 35”> “Watershed” > “Analyze Particles- size 60-500”. Each movie was bleach-corrected for exponential decay, and the mean intensity of each ROI was computed over all time frames (Fiji). After assigning each cell to its morphoclass, we proceeded with the network analysis in MATLAB (MathWorks Inc). The calcium transient detection method was modified from the original script: the fluorescent values were smoothed using a moving average over 7 points, and the baseline fluorescence (F0) was calculated by identifying the minimum value within a 100-points window preceding the time point of interest. Finally, ΔF/F0 (DFF) was calculated. A spike was detected when the peak height exceeded 4 times the standard deviation of all DFF values in the movies. The parameters of the network analysis were adapted from (*48*) as follows: cells were considered active with 1 peak within our 3 minutes movies; periodic cells were defined with more than 3 firings within the 3 minutes movies; trigger cells must excite at minimum 2 cells and hub cells must correlate with more than 4 cells.

Temozolomide resistance assays

Onda -11 GSCs were grown as previously described (*16*). They were metronomically treated with 200 µM Temozolomide (TMZ) (Sigma Aldrich, T2577) every 48h for 7 days to select the resistant GSC morphoclasses. Bright field images were taken to quantify the proportion of GSC morphoclasses at day 7.

For TMZ titration in GBM organoids, we treated the organoids for 96 h with doses ranging from 200 µM to 5000 µM. Viability was assessed with the CellTiter-Glo® 3D (Promega, G9681) and the luminescence was normalized on the area of the organoids and on the vehicle. To select the GSC population resistant to TMZ, GBM organoids were metronomically treated with 200 µM, 500 µM Temozolomide (TMZ) (Sigma Aldrich, T2577) or DMSO in GBM organoid medium every 48 hours for 10 days. At day 10 they were fixed in 4% PFA and processed into 20 µm cryosections for immunofluorescence. Organoids from 4 different patients were used in three independent experiments with 3 organoids per patient for each patient in each experiment.

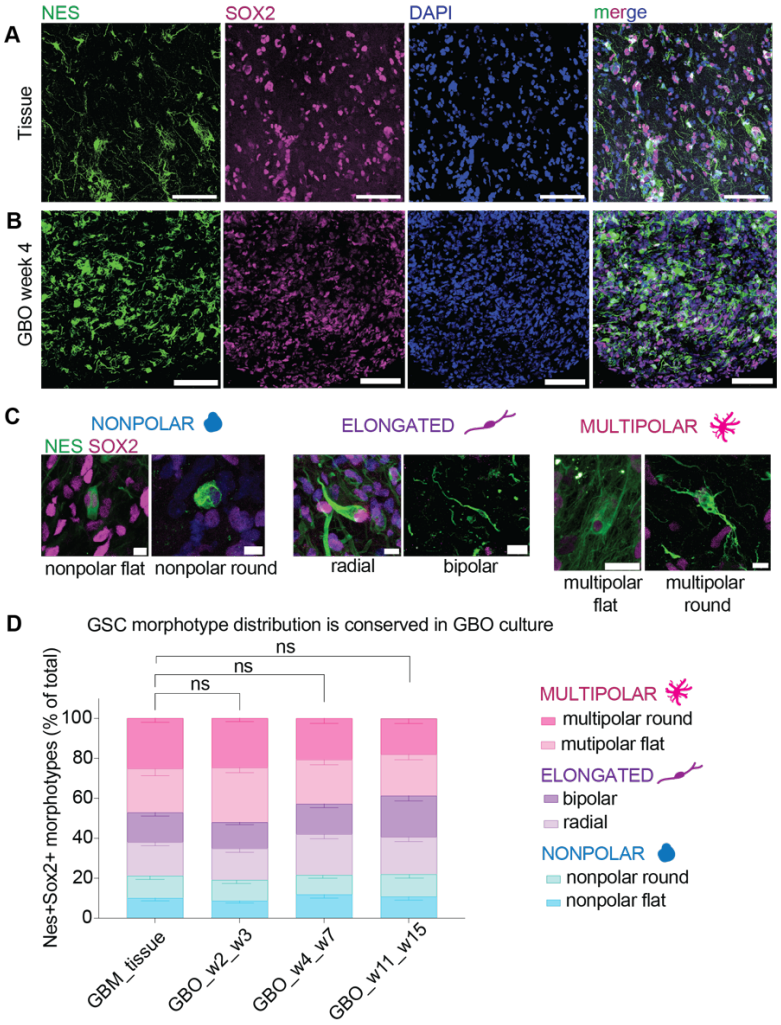

Fig. 1. GSCs are morphologically heterogenous in patient-derived tissue and organoids. (A-B) Representative microscopy images of Nes+ SOX2+ GSCs exhibiting different morphologies in patient primary tissue (A) and patient-derived glioblastoma organoid (GBO, B). Scale bars, 100 µm. (C) Representative microscopy images of the six Nes+ SOX2+ GSC morphotypes grouped into three morphoclasses. Nonpolar cells comprise nonpolar flat and nonpolar round; elongated comprise radial and bipolar; multipolar comprise multipolar flat and round. Scale bars, 10 µm. (D) Quantitative analysis of the distribution of GSC morphotypes and morphoclasses in tissue and GBM organoids (GBO) at different culture timings. Morphotype distribution is not altered upon organoid culture. Error bars, SEM; n=4 patients, 3+ organoids per patients, 3 fields of view per organoid/tissue section.

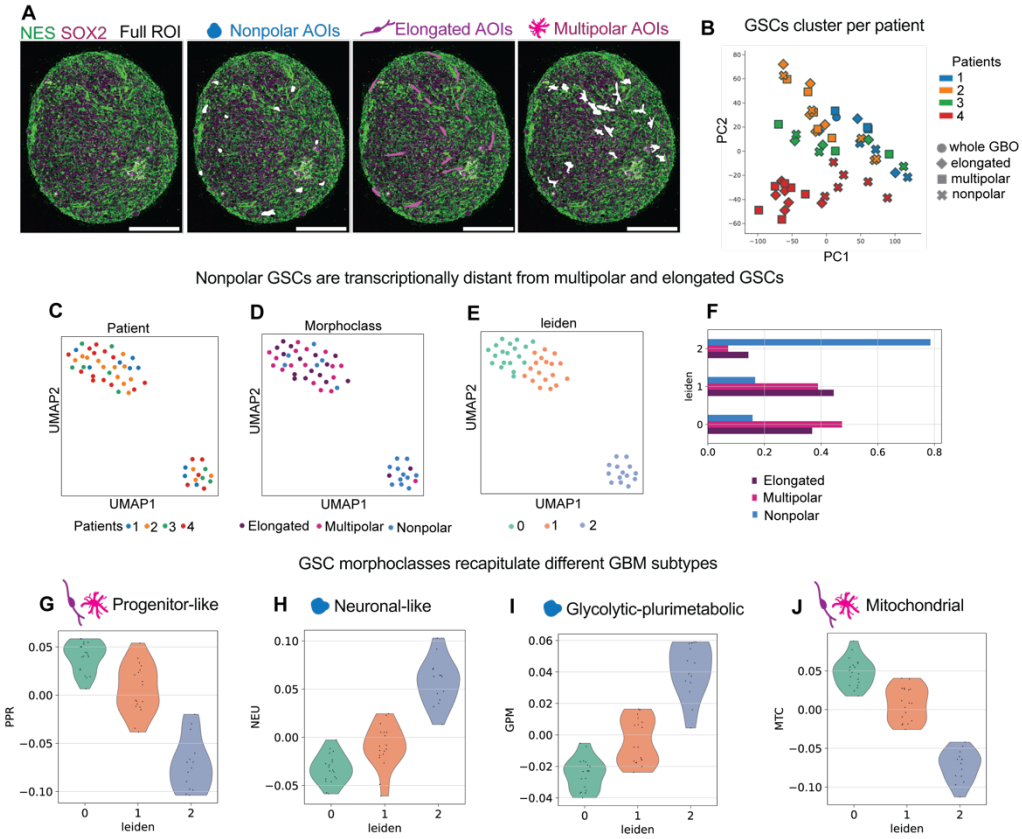

Fig. 2. GSCs have morphoclass-specific transcriptomic signatures.
(A) Custom spatial transcriptomics approach to select cells based on their morphology. Representative image of a GBM organoid (full region of interest, ROI) stained with Nestin and SOX2 and acquired with the Nanostring GeoMX platform to identify the Areas of interest (AOIs, cell segmentations of the same morphoclass). AOI segmentations for nonpolar, elongated and multipolar GSCs. Scale bars, 500 µm. (B) Dimensionality reduction of the GeoMX data. Principal Component Analysis (PCA) plot of the expression profiles of the AOIs from the GeoMX experiment on the GBM organoids. Colors indicate the patient from whom the organoid was derived, while symbols represent different morphoclasses (gray in the legend). (C-F) Clustering of the pathway deconvolution analysis results. Uniform Manifold Approximation and Projection (UMAP) plot of pathway deconvolution results for each AOI, computed as described in the Methods section. The three panels (C-E) show coloring by patient (C), morphoclass (D), and clusters computed with Leiden algorithm (E). The accompanying bar plot displays the number of AOIs per cell type within each cluster (F). (G-J) Functional scores of the pathway deconvolution clusters. Violin plots depicting different functional scores— Progenitor-like (G), Neuronal-like (H), Glycolytic-plurimetabolic (I), and Mitochondrial (J)—grouped by Leiden clusters. Functional scores for each AOI were computed by averaging pathway enrichment values over the pathway classes described in (*9*).

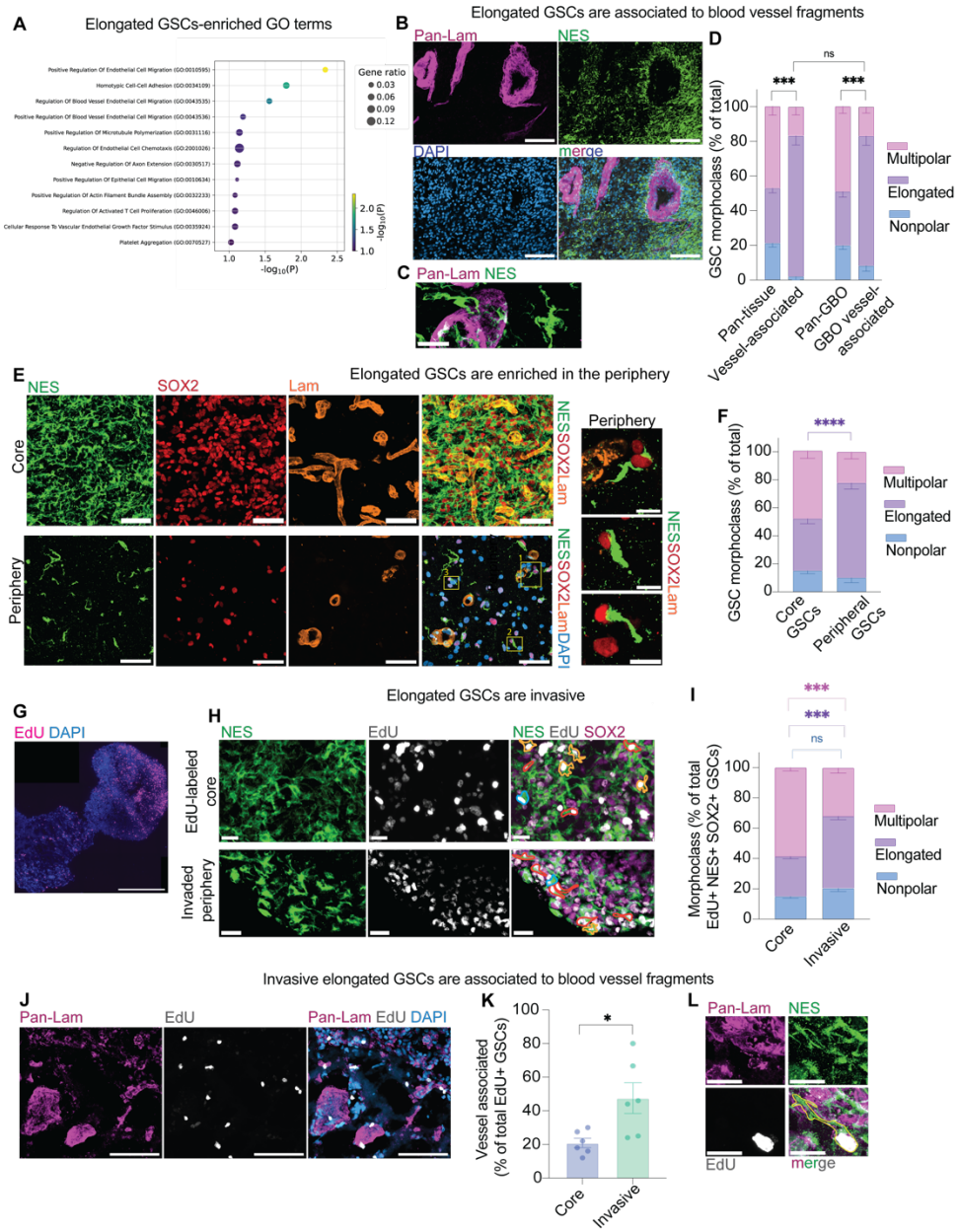

Fig. 3. Elongated GSCs are invasive and associated to blood vessels.
(A) Enrichment of selected Gene Ontology (GO) Biological Process (BP) terms in elongated cells. In the plot, the x-axis position and dot color represent the significance level of the pathway enrichment, while the dot size indicates the proportion of genes associated with each GO term that are differentially expressed in our analysis. Just some selected GO terms which we functionally validated were selected (view full graph in fig. S3B). (B-D) Elongated GSCs are associated to blood vessel fragments. (B) Representative microscopy images of Nes+ GSCs in the parenchyma and associated to Laminin+ blood vessel fragments. Scale bar, 100 µm. (C) Close-up of an elongated cell associated to a Laminin+ vessel and a multipolar cell in the parenchyma. Scale bar, 20 µm. (D) Quantitative distribution of the three morphoclasses associated to the blood vessel fragments compared to the overall distribution in tissue and GBM organoids (GBO). N=4 patients. ****, P<0,0001. (E-F) Elongated GSCs are enriched in the periphery of the primary tumor. (E) Representative microscopy image of core (top) and

peripheral (bottom) patient GBM tissue stained with Nestin (green), SOX2 (red), Laminin (orange) and DAPI (blue, in the merge). Elongated GSCs are enriched in the periphery (see the three close ups). Scale bars, 100 µm (F) Quantitative distribution of the three morphoclasses in patient tissue sections of the core and periphery of the tumor. N=5 patients. ****, P<0,0001. (G-I) Elongated GSCs are invasive. (G) Representative microscopy image of one assembloid with EdU+ (magenta) core organoid fused with a peripheral organoid invaded by EdU+ GSCs. Scale bar, 500 µm. (H) Nes+ SOX2+ EdU+ cells in the core and peripheral part of the assembloid have different morphologies (cell segmentations in colors: red-elongated, blue-nonpolar; orange-multipolar). Scale bars, 20 µm. (I) Quantitative distribution of EdU+ Nes+ SOX2+ morphoclasses in the core and in the invaded part of the assembloid. N= 21 assembloids. ****, P<0,0001. (J-L) Invading elongated GSCs are associated to blood vessels. (J) Representative microscopy image of EdU+ invading cells associated to Laminin+ vessels. Scale bar, 100 µm. (K) Quantification of EdU+ GSCs associated to the vessels in the core and in the invaded part of the assembloid. N=6 assembloids from 3 different patients. *, P= 0,0189. (L) Representative microscopy image of an elongated invasive EdU+ GSC associated to a vessel. Scale bar, 20 µm.

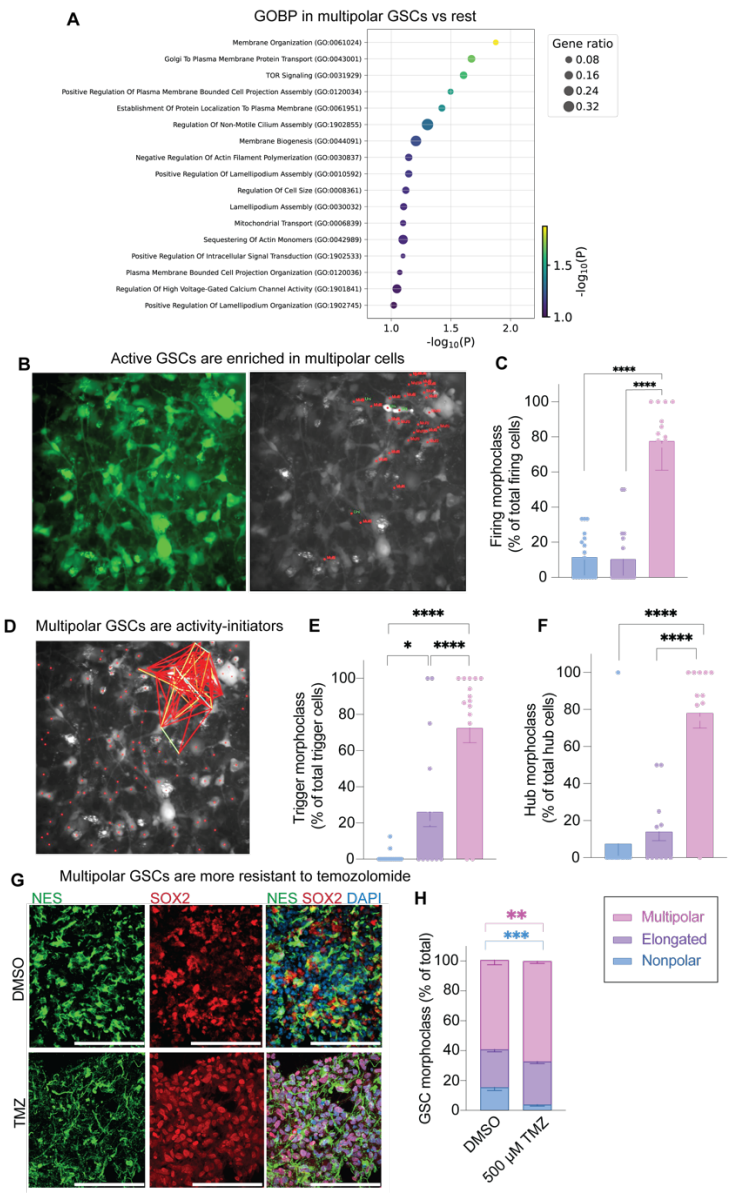

Fig. 4. Multipolar cells form a functional resistant network.
(A) Enrichment of selected Gene Ontology (GO) Biological Process terms in multipolar cells. In the plot, the x-axis position and dot color represent the significance level of the pathway enrichment, while the dot size indicates the proportion of genes associated with each GO term that are differentially expressed in our analysis. Just some selected GO terms which we functionally validated were selected (view full graph in fig. S4B). (B, C) Multipolar cells are the most active. (B) Max intensity projection (MIP) of the live Fluo4 calcium imaging movie. Frame width, 389 µm. Morphoclass label in active cells (red, multipolar; green, elongated). (C) Quantification of firing morphoclasses over total firing cells. ****, P<0,0001. N=39 organoids from 6 different patients. (D-F) Multipolar cells are activity-initiators. (D) Example of connectivity map starting from a hub cell and spreading to neighboring cells. Frame width, 389 µm. (E, F) Quantitative distribution of trigger morphoclasses over total trigger cells (E) and of hub morphoclasses over total hub cells (F). *, P<0,01; ****, P<0,0001. N=39 organoids from 6 different patients. (G, H) Multipolar GSCs are resistant to temozolomide (TMZ). (G) Representative microscopy image of GBM organoids treated with 500 µM TMZ (bottom) and DMSO control (top) stained with Nestin (green), SOX2 (red) and DAPI (blue). Scale bars, 100 µm. (H) Quantitative distribution of GSC morphoclasses in GBM organoids treated with

DMSO and 500 µM TMZ. Multipolar cells**, P<0,01; Nonpolar GSCs***, P<0,001. N=3 experiments with 4 different patients.